Parameter investigations on lithium-niobate-based photonic crystal optomechanical cavity

Dingwei Chen, Sohail Muhammad, Wenyi Huang, Xiang Zheng, Guangjun Wen, and Yongjun Huang*

School of Information and Communication Engineering, Sichuan Provincial Engineering Research Center of Communication Technology for Intelligent IoT, University of Electronic Science and Technology of China, Chengdu, 611731, China
Corresponding author: yongjunh@uestc.edu.cn

Abstract: In this paper, to fully understand the influence of nanofabrication error issues on the lithium-niobate-based device, the systematic simulations and optimizations of lithium-niobate-based photonic crystal (PhC) optomechanical cavity considering the material dispersion and inclination angle of PhC air hole are investigated in details. The structural parameter influences on the PhC band gap, the line defected waveguide transmission characteristics, the optical resonant wavelength of the PhC microcavity, and the mechanical resonant frequency are all discussed. The effects of the simulation methods on the PhC band gap are investigated as well. And finally, the opto-mechanical coupling rate of the lithium-niobate-based PhC optomechanical cavity structure is calculated. Such obtained results can help researchers to precisely design the required optomechanical cavity for specific applications.

本文为充分理解纳米加工误差问题对铌酸锂基器件的影响，对考虑 PhC 气孔材料色散和倾角的铌酸锂基光子晶体（PhC）光机械腔进行了系统仿真和优化。讨论了结构参数对 PhC 带隙的影响、线缺陷波导传输特性、PhC 微腔的光学谐振波长和机械谐振频率。还研究了仿真方法对 PhC 带隙的影响。最后，计算了铌酸锂基 PhC 光机械腔结构的光机耦合速率。这些获得的结果可以帮助研究人员精确设计特定应用所需的光机械腔。

Keywords: Lithium-Niobate, photonic crystal cavity, optomechanical cavity

Introduction

Cavity optomechanics [1,2] is a rapidly developed research area with exciting classic [3,4] and quantum [5,6] mechanical investigations, and has many practical applications. For examples it can be used to make highly sensitive and wide bandwi dth sensors [7] such as the detection or sensing of motion [8], force [9], mass [10], acceleration [11], and magnetic field [12]; and it can also be used to manufacture optical extension lines [13] and tunable filters for integrated microwave oscillators and optical signal processing. In the research progress of cavity optomechanics, a variety of architectures for optomechanical cavity realizations have been proposed, including microdisks [14], microrings [15], microspheres [16], two-dimensional photonic crystals (PhC) [17-19], and nanobeams [20-22], etc. There is also a wide choice of thin film materials used to implement optomechanical cavity, including silicon [23,24], silicon dioxide [25,26], silicon nitride [27], silicon carbide [28], and gallium arsenide [29], etc. In particular, in the wavelength range of ~795 nm for some special applications such as the chip scale atomic clock (CSAC) based on the coherent population trapping (CPT) mechanism [30], the optical losses of conventional film materials like silicon and silicon dioxide in such wavelength range are too high, and other new film materials with lower optical losses, e.g., lithium niobate and silicon nitride are better choices. For the mentioned CSAC, one can use the PhC cavity optomechanical system as the reference source [31], while it should also work in the 780-800nm wavelength range. Therefore, the lithium niobate is one of the good candidates.

In recent years, more specifically, the 780-800nm wavelength range has played an increasingly important role in atomic physics and quantum optics, with applications such as manipulation and cooling of rubidium atoms [32], frequency standards [33] and quantum

47 storage [34], etc. Our research about lithium-niobate-based photonic crystal optomechanical
48 cavity can be combined with the CSAC architecture [35,36] for frequency standards. The
49 conventional CSAC uses microwave signal generated by the MEMS oscillator to control the
50 frequency difference between two coherent laser beams. The CPT occurs when the microwave
51 frequency is close to the jumping frequency between the two hyperfine energy levels of the
52 atomic ground state, resulting in a highly accurate standard frequency signal. However,
53 conventional MEMS oscillators suffer from high power consumption, complex systems and
54 low reliability. Using photonic crystal optomechanical cavity instead of MEMS oscillator for
55 frequency standards can effectively avoid those problems. In the future, we plan to combine
56 rubidium gas chamber with cavity optomechanical system and the excitation laser wavelength
57 required for the D1 hyperfine splitting energy level jumping of rubidium (87Rb) atoms is
58 794.9789 nm [37]. Therefore, the emphasis of this study lies on the design of lithium-niobate-
59 based photonic crystal optomechanical cavity operating in the ~795 nm wavelength range and
60 the influence discussion of structural parameters on cavity optomechanical cavities.

61 On another hand, as an emerging material with excellent properties (strong photoelectric
62 effect, stable physical and chemical properties, and wide range of light transmission with low
63 loss), lithium niobate is widely used in optics areas, including waveguide amplifier [38],
64 microwave synthesizer [39], electro-optic modulator [40,41] and on-chip laser [42]. The high-
65 quality PhC cavity based on lithium niobate has also been reported in recently years [43,44].
66 However, current PhC cavities are mainly worked at the ~1550 nm wavelength range, and the
67 PhC nanocavity working in the ~795 wavelength range has not been reported so far. Most
68 importantly, the performances of the PhC nanocavities are far from the design goal due to the
69 high hardness properties of lithium niobate and the deficiencies of the processing technology,
70 which has been one of the key issues.

71 As a result, so far there are few systematic studies on the cavity optomechanical structure
72 based on lithium niobate photonic crystal nanocavity [45-47], and there is no systematic
73 simulation investigation considering the impact of nanofabrication errors on the
74 optomechanical cavity properties. In this paper, the influences of structural parameters on
75 optical and mechanical properties of lithium-niobate-based PhC cavity optomechanical
76 structures are analyzed systematically. Starting from the high-precision simulations of lithium-
77 niobate-based PhC slab design considering both thickness and dispersion, the effect of
78 predictable nanofabrication processing errors (especially the tilt angle of nanohole wall) on the
79 performance of the cavity optomechanical structure is investigated. The influences of different
80 simulation methods in FDTD on the simulation results are also discussed. Lastly, the solution
81 for preventing the nanofabrication processing errors in the final fabricated optomechanical
82 cavity is provided. Based on the obtained results in this paper, the researchers can rapidly and
83 accurately design and optimize lithium-niobate-based PhC cavity optomechanical structures to
84 meet their demands, and the influences of nanofabrication errors on the nanocavities can be
85 avoided in advance during the design processes.

Lithium-niobate-based PhC optomechanical cavity under consideration

87 The lithium-niobate-based PhC optomechanical cavity studied in this paper is shown in Fig.
88 1(a) which contains: photonic crystal slab, line defect waveguide with air slot, hole shift for
89 achieving high-quality nanocavity, and large-area square defect to form the typical
90 optomechanical cavity configuration. Specifically, the PhC nanocavity structure shown in Fig.
91 1(b) is composed of three different air hole perturbations, line defect and air slot, which is a
92 classic cavity configuration and has been widely discussed before [48-50]. The square defect
93 structure allows the structure to undergo mechanical oscillations at a certain radio frequency.
94 The working principle of the cavity optomechanical system is shown in Fig. 1(c) [1,2]. When
95 the light with intensity reaching a certain level acts on the nanocavity, the optical radiation
96 pressure can drive the reflection mirror connected to a spring at one end to vibrate, resulting in
97 a changing in the resonant cavity field and a changing of the optical resonant frequency, thus

98   achieving a mutual coupling between the resonant cavity optical field and the mechanical
99   oscillator vibration.
100   Based on the above short introduction, Fig. 1(d) shows the SEM of lithium-niobate-based
101   PhC optomechanical cavity that we previously designed after the initial simulations and
102   processed by reactive ion etching method. And Fig. 1(e) shows the cross-sectional view of the
103   air hole of this chip structure, in which we noticed that due to the material properties of lithium
104   niobate and the limitations of the processing technology, the processing of round holes on
105   lithium niobate material often results in obvious wall inclination. So this fabricated sample is
106   unable to meet the initial design expectation for further optomechanical cavity characterizations.
107   Therefore, in the rest of this paper, we would like to investigate the influences of structural
108   parameters and processing errors on optical and mechanical properties of lithium-niobate-based
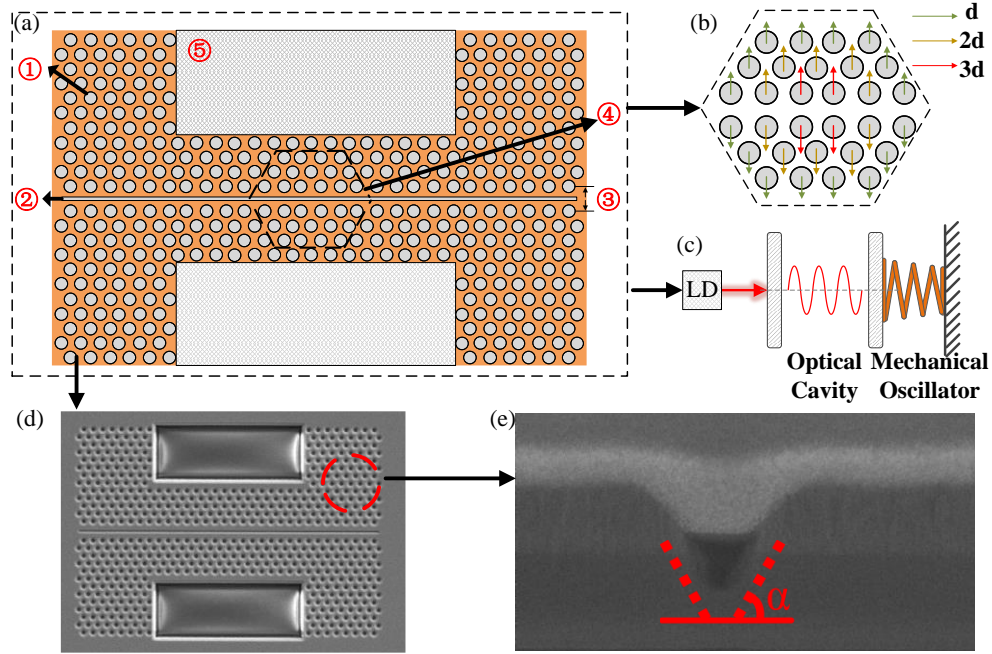109   PhC cavity optomechanical structures.

Fig. 1 (a) Two-dimensional PhC cavity optomechanical system based on lithium niobate, (b)
resonant cavity constructed by tertiary perturbation, (c) working principle of the cavity
optomechanical system, (d) the SEM diagram of the cavity optomechanical device, and (e) the
SEM diagram of air holes with obvious inclination (side view).

Investigations on the lithium-niobate-based PhC cavity

116   Firstly, as shown in Fig. 2(a), the optical transparent window of silicon is 1.1-5 μm, while
117   lithium niobate is 0.35 -5.5 μm. As we need to design the PhC cavity structures working in both
118   ~795 nm and ~1550 nm ranges, we choose lithium niobate as the material of optomechanical
119   cavity. The band gap is the most important feature of PhC, and in order to analyze the influence
120   of various PhC structure parameters on the band gap, the commercial software FDTD solution
121   is used in this section to calculate the band gap of lithium-niobate-based PhC structures. The
122   main structural parameters used in the FDTD simulations include the refractive index n of the
123   material constituting the PhC structure, the lattice constant a of the PhC slab, the air hole radius
124   r and the thickness z of the PhC slab. The effect of the hole wall inclination angle $α$ on the band
125   gap is discussed in next section.

126   *A. Building for FDTD simulation model*

127 Based on the finite difference time domain (FDTD) method, the unit cell of PhC slab is meshed
128 by the two-dimensional finite difference method [51,52]. The space step Δx, Δy and Δz in three
129 directions, and the time step Δt must meet the stability conditions [46]:

$$130 \qquad c\Delta t = \frac{1}{\sqrt{\dfrac{1}{x^2} + \dfrac{1}{y^2} + \dfrac{1}{z^2}}} . \qquad (1)$$

131 In order to meet the stability conditions, the values of the space and time steps need to be
132 extremely small; and in order to meet the design requirements of PhC structures, a large number
133 of structures need to be simulated. For this reason, simulation of PhC structures is time-
134 consumed. To improve the simulation efficiency, we exploit the periodic properties of PhC in
135 the XOY plane, and use Bloch boundary conditions for the x and y directions and PML for the
136 z direction. The established FDTD model is shown in Fig. 2(b). And the structure is based on
137 z-cut lithium niobite thin film. Based on the model shown in Fig. 2(b), we investigate the
138 relationship between the band gap of the PhC slab and parameters a, r, and z. In addition, the
139 influences of the simulation model setting method on the band gap simulation results and the
140 effect of the hole wall inclination (shown in Fig. 2(c)) on the band gap are investigated as well.
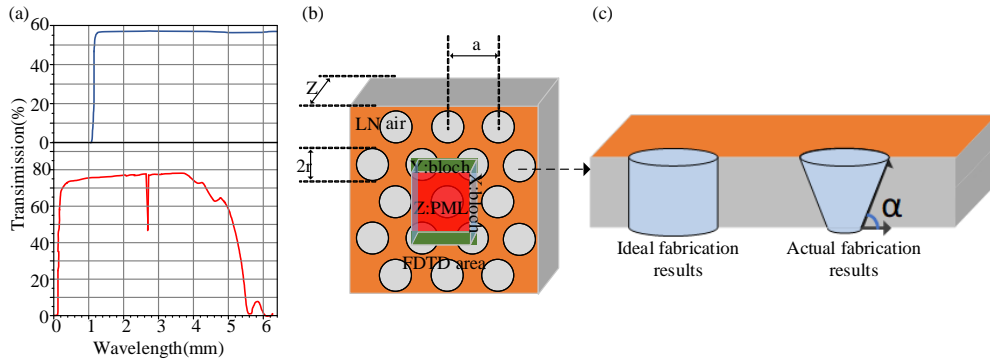

141

142 Fig. 2 (a) Transmittance spectrum of silicon and lithium niobate, (b) photonic crystal band gap
143 simulation model, and (c) comparisons of ideal machined air holes and actual fabricated air holes.

B. Parameter study on lattice constant

145 To study how the lattice constant a affects the band gap performances, the model is simulated
146 under three different $a{:}r{:}z$ conditions with the PhC lattice constant a as variable parameter, and
147 the model is simulated at two different levels of PhC lattice constants (290-380 nm and 575-
148 825 nm) in order to avoid the effect of different operating bands of the PhC on the results. Also,
149 those two kinds of lattice constant levels correspond to the two operating wavelength ranges,
150 namely ~795nm and ~1550 nm. Firstly, the modeled normalized band gap width $\Delta\omega/\omega_{center}$ and
151 the center of the normalized band gap $\omega_{center}/2\pi c$ as functions of the lattice constant a are shown
152 in Fig. 3(a) and (b). In those figures, $\Delta\omega/\omega_{center}$ and $\omega_{center}/2\pi c$ are independent of lattice
153 constant. $\Delta\omega/\omega_{center}$ and $\omega_{center}/2\pi c$ vary less with the increasing of lattice constant a when the
154 ratio of the structural parameters keeps constant. These slight variations are usually caused by
155 the simulation errors as well as by the lattice division. Therefore, in Fig. 3(a) and (b), only the
156 result for the ~1550 nm case is presented.

C. Parameter study on air hole radius

158 By using the same analysis method as shown in above subsection, the band gap is simulated
159 for three different $z{:}a$ conditions which use the air hole radius r as variable parameter. The
160 modeled band gap performances versus the air hole radius $r(a)$ are shown in Fig. 3(c)-(f). From
161 those plots, it can be found that width and center of the photonic crystal band gap and the air
162 hole radius have positive correlation for all z/a conditions. Also we notice that for both ~795
163 nm and ~1550 nm conditions, the band gap width varies less when $r/a > 0.35$.

164 *D. Parameter study on slab thickness*
165 Moreover, the modeled band gap width versus the lithium niobate slab thickness $z(a)$ are shown
166 in Fig. 4(a) and (c), where it can be found that the band gap width firstly increases with the
167 increasing of z/a, then keeps near constant, and finally decreases rapidly, for both ~795 nm and
168 ~1550 nm conditions. Also, the starting point of z/a for a rapid decrease in band gap width have
169 a negative correlation with r/a. For example, in the 1550 nm condition (Fig. 4(c)), the decrease
170 start point of band gap width are z/a=1.6, z/a=1.45 and z/a=1.15 for r=0.28a, r=0.35a and
171 r=0.42a, respectively. This is because for a PhC flat slab, if the slab is too thin, the frequency
172 difference between the first-order conduction band and the light cone becomes too small,
173 whereas as the slab thickness starts to increase, the higher-order modes move to lower
174 frequencies and enter the band gap. At some points the higher order modes are pushed into the
175 bandgap so that the bandgap starts to decrease abruptly. On the other hands, the modeled band
176 gap center positions are shown in Fig. 4(b) and (d), from which it can be seen that the
177 normalized bandgap center decreases as z/a increases when r/a is determined.
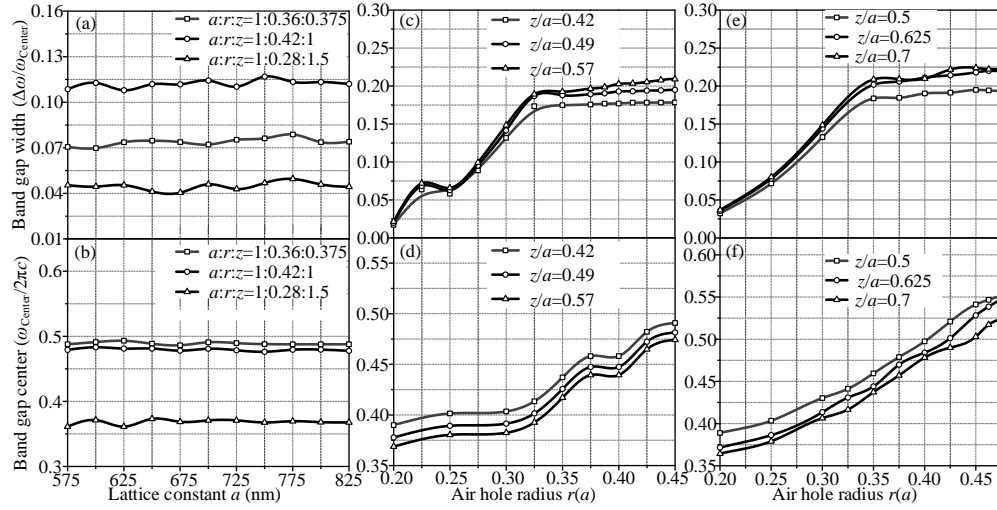
178

179 Fig. 3. The normalized band gap width $\Delta\omega/\omega_{center}$ and the center of the normalized band gap
180 $\omega_{center}/2\pi c$ (a)(b) as the function of lattice constant a for ~1550 nm band; (c)(d) as the function
181 of air hole radius $r(a)$ in the ~795 nm band; and (e)(f) as the function of air hole radius $r(a)$ in
182 the ~1550 nm band.

183 Based on the simulation analysis results in subsections from 3.2 to 3.4, we can get the
184 optimized wide-bandgap lithium-niobate-based photonic crystal structures operating in the
185 ~795nm wavelength range and ~1550nm wavelength range, respectively. The final optimized
186 band gaps are shown in Fig. 4(e) and (f). For Fig. 4(e), the lattice constant is 335 nm, and
187 a:r:z=1:0.375:0.675. And for Fig 4(f), the lattice constant is 660nm, and a:r:z=1:0.35:0.8.

188 *E. Effect of dispersion on band gap simulation*
189 When designing PhC structures, it is necessary to simulate a large number of structures to meet
190 specific requirements. Therefore, improving the simulation efficiency of the photonic crystal
191 band structure is conducive to structure design. Using the FDTD simulation method, the lattice
192 constant a, radius r, thickness z, and the refractive index n of the material are enough to get the
193 basic band structure results, additionally, in order to obtain more accurate results, the dispersion
194 of the lithium niobate material also need to be considered. When considering the dispersion,
195 the lithium niobate material has birefringence features, and its refractive index is given in the
196 form of Sellmeier equation [53]:

197
$$n_o^2 = 4.9048 - \frac{0.11768}{0.0475 - \lambda^2} - 0.27169\lambda^2 . \qquad (2)$$

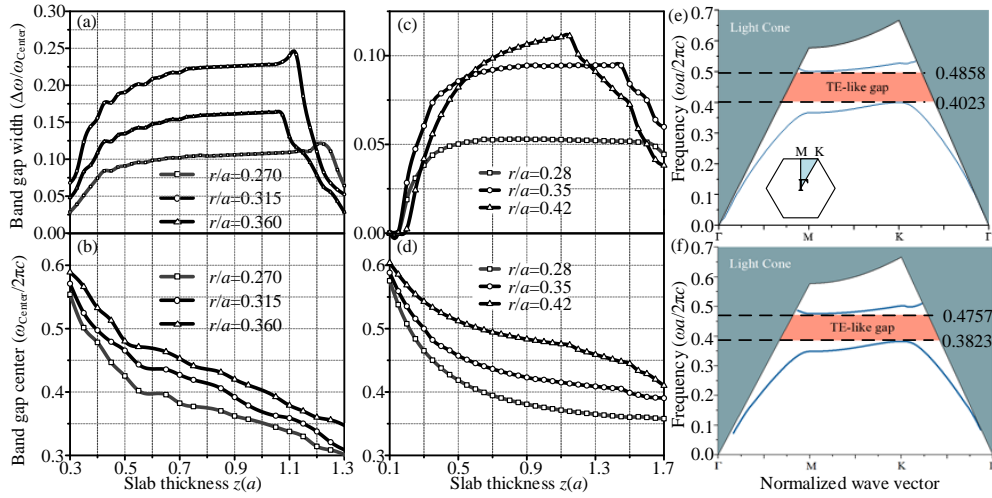$$n_e^2 = 4.582 - \frac{0.099169}{0.044432 - \lambda^2} - 0.02195\lambda^2 . \qquad (3)$$

Fig. 4. The normalized band gap width $\Delta\omega/\omega_{center}$ and the center of the normalized band gap $\omega_{center}/2\pi c$ as the function of slab thickness z(a) for (a)(b) ~795 nm and (c)(d) ~1550 nm conditions, and (e)(f) the optimized band gaps for the lithium-niobate-based photonic crystal structures centered at ~795 nm and ~1550 nm, respectively.

For different PhC structures, the computational complexity of the high-precision model is 2 to 5 times than basic model. We compared the effect of models with different simulation settings on the bandgap structure and the results are shown in Table 1.

Table. 1. Effects of different simulation model settings on normalized band gap center and normalized band gap width

Group \ Model	A-width	A-center	B-width	B-center	C-width	C-center	D-width	D-center
1	0.0958	0.431	0.0934	0.429	0.0382	0.401	0.0434	0.533
2	0.0599	0.426	0.0611	0.427	0.0324	0.388	0.0377	0.528
3	0.0514	0.379	0.0527	0.381	0.0345	0.382	0.0401	0.512
4	0.0517	0.370	0.0511	0.374	0.0326	0.370	0.0348	0.506

In Table 1, we analyze the influence of model settings on the normalized bandgap width and the normalized bandgap center position for four structures, where A and B are wide-bandgap structures, C and D are narrow-bandgap structures. Simulations were performed under 4 different model settings. Model 1 is a high-precision model that incorporates both dispersion and slab thickness into the calculation. Model 2 is a model that does not consider dispersion but considers thickness. Model 3 does not consider thickness but considers dispersion. Model 4 is a basic model which does not consider dispersion and thickness. By comparing each model with model 1 we can conclude that ignoring dispersion has less impact on the calculation of the band gap center but results in a significantly smaller band gap width than the actual value. For wide band gap structures, ignoring thickness can lead to significant deviations in both results. And for narrow band gap structures, although the width of the band gap is less affected, the deviation of the center position of the band gap is still large. Therefore, in order to improve the simulation efficiency while ensuring the accuracy of the results, the center position of the band gap can be approximate calculated by using a photonic crystal model that does not consider dispersion. After that, the bandgap width can be determined precisely through a complete model simulation.

225 *F. Air hole wall inclination*
226 Lastly, based on the above established precisely numerical investigation method, effect of the
227 wall inclination on the band gap performances can be discussed. As mentioned in Introduction
228 section, when processing the photonic crystal flat slabs with nanofabrication methods such as
229 electron beam lithography (EBL), reactive ion etching (RIE) and focused ion beam (FIB) to
230 etch the air holes on the photonic crystal flat slabs, the processed air hole wall will have a
231 certain angle with the horizontal plane. The schematic view and real fabricated sample are
232 presented in Fig. 2(c) and Fig. 1(e). For the photonic crystal slab structure and the microcavity
233 structure with hole shift perturbations, the inclination of the air hole wall has a certain influence
234 on the band gap performances and the optical waveguide and cavity properties. For example,
235 when designing a photonic crystal line defected waveguide, the inclination of the hole wall may
236 lead to a change in the position of the band gap, making the operating band of the waveguide
237 not meet the wavelength requirements. Therefore, numerically investigating the effect of the
238 inclination of the air hole wall on the band gap can help to minimize the impact of processing
239 errors on the performance of photonic crystal flat slabs when designing photonic crystal chip
240 layouts.
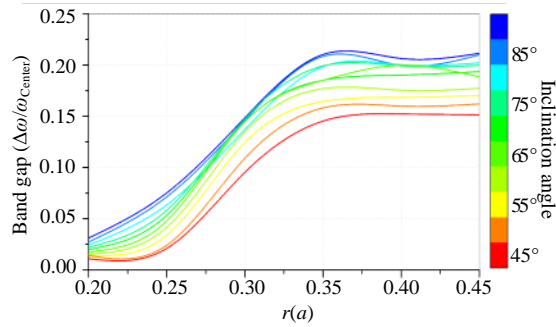
241

242 Fig. 5. The effects of different inclination angles on the band gap width under different $r(a)$.

243 The numerically investigated effect of the photonic crystal hole wall inclination on the
244 normalized bandgap width is shown in Fig. 5 (z:a=0.675). It can be found that as the tilt
245 increases (namely the inclination angle decreased from 90° to 45°), the maximum band gap
246 width is decreased, which is reflected from Fig. 5 that the overall downward shift of the curves.
247 Specifically, when the inclination angle is reached 45°, the band gap width is reduced by about
248 40%. At the same time, the normalized band gap center position is shifted by 5% to 10%.
249 Therefore, when designing the lithium-niobite-based photonic crystal cavity chip, the effect of
250 the hole wall inclination on the performance of the PhC slab needs to be fully considered.

251 **Demonstrations of lithium-niobate-based PhC optomechanical cavity**

252 In this section, we further combine COMSOL with FDTD Solution to simulate the transmission
253 characteristics of lithium-niobate-based PhC line defected waveguide, the relationship between
254 optical modes and structural parameters of lithium-niobate-based PhC microcavity, and the
255 mechanical modes and opto-mechanical coupling rates of the lithium-niobate-based PhC
256 optomechanical cavity. Since the simulation process is the same for the cavity optomechanical
257 structures of different wavelength, only the results for ~1550 nm wavelength range are
258 simulated in this section.

259 *A. Waveguides transmission characteristics simulations*
260 When designing lithium-niobate-based PhC microcavity, the first step is to design the PhC line
261 defect waveguide, which needs to ensure that the operating wavelength range of the PhC
262 waveguide contains the required wavelengths, e.g., ~795 nm and ~1550 nm. In order to simulate
263 the transmission characteristics of the lithium-niobate-based PhC waveguide, a model has been
264 constructed as shown in Fig. 6(a). We place the light source on a straight waveguide outside

265 the photonic crystal structure. The traditional method of monitoring waveguide transmission in
266 FDTD solution is to place a monitor near the end of the waveguide and compare the monitored
267 light intensity with that of the light source to obtain the transmission spectrum. However, since
268 our light source is located outside the structure, some loss of energy occurs when the straight
269 waveguide couples with the PhC line defected waveguide. Therefore, two monitors were set
270 inside the PhC line defected waveguide, as shown in 6(a), where T1 is located at the beginning
271 of the PhC line defected waveguide and T2 at the end of the waveguide. Light intensity entering
272 the PhC line defected waveguide is monitored through the T1 monitor and the optical spectrum
273 measured by the T1 monitor is taken as the initial light intensity. The optical spectrum measured
274 by the T2 monitor is taken as the output light intensity, at which point the transmission at the
275 desired wavelength is equal to the ratio of the light intensities of T2 and T1 at that wavelength.
276 In Fig. 6(b), wavelength region where T2/T1 is greater than 0.9 are regarded as the operating
277 wavelength band of the PhC line defected waveguide. In Fig. 6(b) a wide pass band from ~1590
278 nm to 1790 nm centered at 1690 nm was obtained. This center wavelength is far away from the
279 anticipated ~1550 nm.

280　　Furthermore, the relationship between the line defect width and the operating wavelength
281 of the lithium-niobate-based PhC line defected waveguide is also analyzed and the results are
282 shown in Fig. 6(c) (colored bars). In addition, effect of the inclination angle of the air hole wall
283 of the PhC on the performance of the PhC line defected waveguide are investigated, and the
284 results are shown in Fig. 6(c) (the overlapping red arrows represent the operating bands affected
285 by the tilt angle). Those results are simulated at a fixed inclination angle of 70°. It can be found
286 that the operating band of the PhC becomes smaller and the center operating wavelength
287 becomes larger as a result of the air hole wall inclination.

288　　Those results further verify that the fabrication errors, especially the existent inclination
289 angle will sharply affect the operating wavelength band and the center operating wavelength.
290 This the main reason that the obtained center operating wavelength is deviated from the ~1550
291 nm if idea structural parameters are chosen. Therefore, based on the above obtained results, we
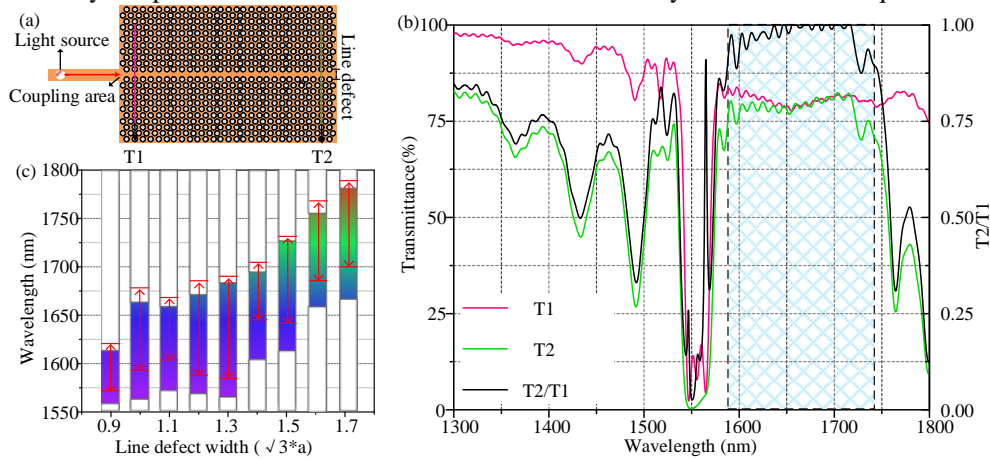292 can easily re-optimized structures to ensure the fabricated cavity is closer to the required one.

293

294　　Fig. 6. (a) Simulation model for the demonstration of transmission spectra of lithium-niobate-
295　　based line defected waveguides (z=300nm), (b) the simulated transmission spectra patterns, and
296　　(c) the influences of line defect width and air hole tilting on waveguide transmission
297　　characteristics.

298 *B. Optical and mechanical modes, and opto-mechanical coupling rate simulations*
299 In order to meet the needs of various experiments and applications, as mentioned in
300 Introduction section, controlling of the optical resonance wavelength of the PhC microcavity
301 and the mechanical resonance frequency of the mechanical oscillator is an important part of the
302 design of cavity optomechanical system. Based on the basic knowledge of cavity

303   optomechanics [1,2], by controlling the input laser wavelength around the optical resonance of
304   the microcavity can excite the mechanical oscillator. Therefore, in this subsection, the optical
305   cavity mode simulations of the lithium-niobate-based PhC microcavity (shown in Fig. 1(b)) are
306   carried out using FDTD solution to calculate the resonant wavelength and Q value of the
307   microcavity by means of an attenuation envelope and a high Q analysis set. The equations are
308   shown below:

309
$$Q = \frac{-2\pi f_R \log_{10} e}{2m} \ .$$
(4)

310   where f_R is the resonant frequency and m is the slope of the attenuation envelope applied in
311   FDTD solution.

312   The discussed PhC structure is based on Fig. 4(f) operated in the ~1550 nm wavelength
313   range. FDTD solution is used to optimize the PhC microcavity and a Q value of 3.2e7 is
314   obtained, whose electric field pattern at resonance wavelength is shown in the inset of Fig. 7(a).
315   This Q value is lower than expected, mainly due to the simulation model setup or simulation
316   accuracy, and it can be seen that there is slight energy leakage outside the PhC microcavity in
317   the figure. Additionally, relationship between the resonant wavelength of this mode and the
318   width of the air slot L or the width of the line defect W has been investigated in this subsection
319   (shown in Fig. 7(a) and (b)) and the results can be used to adjust the optical resonant wavelength
320   during further design. Simulations have also been carried out on the relationship between the
321   resonant wavelength and the tilt angle of the PhC microcavity operating at three different
322   wavelengths, and the results of which are shown in Table 2. It can be found that when the tilt
323   angle is high, there is no optical resonant mode exists. For smaller lattice constant, this
324   phenomenon is more obvious. This is because the tilt of the hole wall causes the band gap to
325   become narrower and lower, making the optical resonant wavelength of the original structure
326   no longer located in the band gap and making it impossible to find an optical mode without
327   changing the structural parameters of the microcavity. For smaller lattice constants, due to the
328   smaller structure scale and narrower band gap, the possibility of the optical resonance
329   wavelength shift out of the band gap range is higher.

330 Table. 2. Effects of tilt angle on optical resonant wavelength

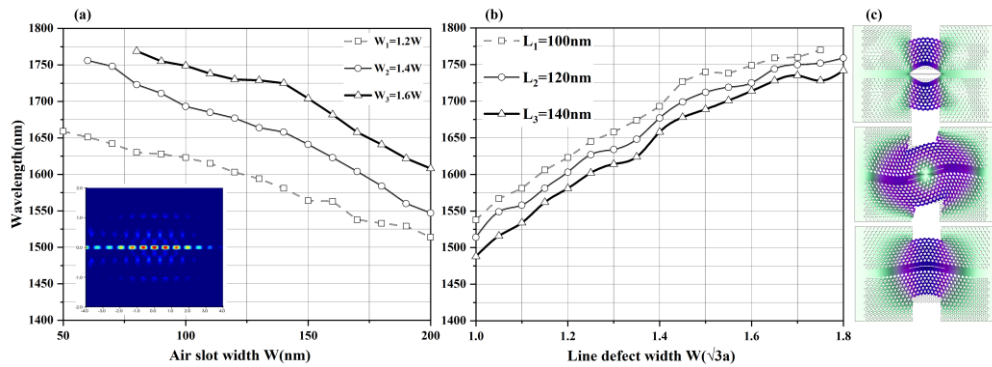| Angle \ Group	90°	85°	80°	75°	70°	65°	60°	55°	50°	45°
1	796.2	804.7	815.6	820.2	/	/	/	/	/	/
2	1102.1	1118.9	1128.4	1135.0	1141.8	1150.3	/	/	/	/
3	1550.8	1558.4	1562.3	1569.5	1577.8	1583.1	1594.8	/	/	/

331

333 Fig. 7. (a) Simulated influences of air slot width on optical resonance wavelength. Inset shows
334 the electric field distribution of the fundamental optical mode. (b) Influence of line defect width
335 on optical resonance wavelength. (c) Simulated partial mechanical mode.

336   Then, mechanical modes of the cavity optomechanical structure shown in Fig. 1(a) are
337 simulated by COMSOL. Three mechanical modes are shown in Fig. 7(c) with mechanical
338 resonance frequencies of 436 MHz, 432 MHz and 405 MHz, respectively. Since the control
339 priority of the optical resonant wavelength and Q value is usually higher than that of the
340 mechanical modes when designing the cavity optomechanical structure, the size of the square
341 defects area and/or the PhC slab size are concerned instead of varying the lattice constant, air
342 hole radius, thickness of the PhC slab, air slot width and line defect width. Results obtained
343 from the COMSOL simulation are shown in Table 3 (the PhC structure on the slab is the same
344 as Fig. 4(f)). As can be seen, by changing the size of the square defect area, the mechanical
345 resonance frequency of the cavity optomechanical structure can be changed in a small range,
346 and while it can be greatly affected by changing the PhC slab size. Therefore, in the actual
347 progress of the opto-mechanical cavity design, the mechanical resonant frequency can be
348 coarsely adjusted by first changing the size of the PhC plate and then fine-tuning the specific
349 mechanical resonant frequency by the square defect area.

350   Table. 3. Effects of square defect size and photonic crystal slab size on the mechanical resonance frequency

Square \ Slab	2μm×2μm	3μm×3μm	4μm×4μm	5μm×5μm	6μm×6μm
10μm×8μm	465.7MHz	488.2MHz	/	/	/
12μm×9.6μm	425.3MHz	447.6MHz	515.7MHz	/	/
15μm×12μm	340.1MHz	355.2MHz	390.8MHz	429.9MHz	/
20μm×16μm	261.7MHz	270.8MHz	284.5MHz	301.6MHz	325.5MHz

351
352   Finally, in the application of cavity optomechanical system, opto-mechanical coupling rate
353 is a vital parameter. The opto-mechanical coupling rate of the lithium-niobate-based PhC cavity
354 optomechanical system are calculated. In a cavity optomechanical system, the opto-mechanical
355 coupling rate can be divided into two parts, one is the photo-elastic effect of stress caused by
356 mechanical motion, which changes the refractive index of the medium, and the other is the
357 equivalent refraction caused by the moving dielectric boundary caused by mechanical motion
358 rate changes, resulting in a change in the optical resonant frequency. For the structure used in
359 this paper, the second factor predominates, the formula for calculating the opto-mechanical
360 coupling coefficient based on the moving boundary is shown as follows [54,55]:

361
$$g_{MB} = \frac{1}{2} \frac{\int dA(\vec{u}(\vec{r}) \cdot \vec{n}) \left[\Delta\varepsilon \left| \vec{E}_{//} \right|^2 - \Delta\left(\varepsilon^{-1}\right) \left| \vec{D}_{\perp} \right|^2 \right]}{\int dV_{\varepsilon} | \vec{E} |^2} \omega_{cav} x_{zpf} \tag{5}$$

362   Among them, the numerator integral is integrated on the moving boundary surface, while
363 the denominator integral is carried out on the entire volume, $\vec{u}(\vec{r})$ is the normalized unitless
364 displacement distribution, so the maximum displacement is 1. Finally, the calculated g_{om}
365 corresponding to the first-order (~805.58 nm), second-order (~799.10 nm) and third-order
366 (~797.23 nm) optical modes are 535 kHz, 492 kHz and 512 kHz, respectively.

367 **Conclusion**
368   In this paper, the complete and systematic numerical investigations of the cavity
369 optomechanical structure based on the lithium niobate PhC cavity are carried out. The
370 relationship between the band gap and structural parameters of PhC is studied, and based on
371 the results, the wide-band-gap lithium-niobate-based two-dimensional PhC slabs operating in
372 the ~795nm and ~1550nm bands are designed. The optical and mechanical properties of two-
373 dimensional PhC cavity optomechanical system based on lithium niobate have been
374 investigated as well. In addition, the influences of air hole wall inclination caused by
375 nanofabrication errors on structural performance (PhC's band gap, waveguide transmission
376 characteristics and optical microcavity resonant wavelength) are all studied in details. Those
377 results obtained in this paper can help researchers to precisely design the required
378 optomechanical cavity by talking the nanofabrication errors into considerations.

390 **Declaration of Competing Interest**

391 The authors declare that they have no known competing financial interests or personal
392 relationships that could have appeared to influence the work reported in this paper.
393

394 **References**

395 1. T. J. Kippenberg, and K. J. Vahala, "Cavity optomechanics: back-action at the mesoscale," Science **321**(5893),
396   1172-1176 (2008).
397 2. M. Aspelmeyer, T. J. Kippenberg, and F. Marquardt, "Cavity optomechanics," Reviews of Modern Physics **86**(4),
398   1391 (2014).
399 3. H.-J. Chen, "The fast and slow light in a hybrid spinning optomechanical system mediated by a two-level system,"
400   Results in Physics, **42**, 105987 (2022).
401 4. Y. Xu, H. Hu, W. Chen, P. Suo, Y. Zhang, S. Zhang, and H. Xu, "Phononic cavity optomechanics of atomically
402   thin crystal in plasmonic nanocavity," ACS Nano **16**(8), 12711-12719 (2022).
403 5. P. Lei, Y. Zhang, J. Cheng, and W.-Z Zhang, "Quantum Toffoli gate in hybrid optomechanical system," Results
404   in Physics, **35**, 105338 (2022).
405 6. S. Barzanjeh, A. Xuereb, S. Gröblacher, et al., "Optomechanics for quantum technologies," Nature Physics **18**,
406   15-24 (2022).
407 7. B.-B. Li, L. Ou, Y. Lei, and Y.-C. Liu, "Cavity optomechanical sensing," Nanophotonics **10**(11), 2799-2832
408   (2022).
409 8. G. A. Brawley, M. R. Vanner, P. E. Larsen, et al., "Nonlinear optomechanical measurement of mechanical
410   motion," Nature Communications **7**, 10988 (2016).
411 9. F. Fogliano, B. Besga, A. Reigue, et al., "Ultrasensitive nano-optomechanical force sensor operated at dilution
412   temperatures," Nature Communications **12**, 4124 (2021).
413 10. J. Liu, and K. D. Zhu, "Room temperature optical mass sensor with an artificial molecular structure based on
414   surface plasmon optomechanics," Photonics Research **6**(9), 867-874 (2018).
415 11. Y. Huang, J. G. Flor Flores, Y. Li, et al., "A chip-scale oscillation-mode optomechanical inertial sensor near the
416   thermodynamic limits," Laser & Photonics Reviews **14**(5), 1800329 (2020).
417 12. B.-B. Li, G. Brawley, H. Greenall, et al., "Ultrabroadband and sensitive cavity optomechanical magnetometry,"
418   Photonics Research **8**(7), 1064-1071 (2020).
419 13. A. Safavi-Naeini, T. Alegre, J. Chan, et al., "Electromagnetically induced transparency and slow light with
420   optomechanics," Nature **472**(7341), 69-73 (2011).
421 14. R. Benevides, M. Ménard, G. S. Wiederhecker, and T. P. M. Alegre, "Ar/Cl 2 etching of GaAs optomechanical
422   microdisks fabricated with positive electroresist," Optical Materials Express **10**(1), 57-67 (2020).
423 15. L. Ren, H. Wen, L. Shi, and X. Zhang, "Electromagnetically induced transparency with a single optomechanical
424   microring resonator," Optics Letters **47**(6), 1363-1366 (2022).
425 16. X. Jiang, M. Wang, M. C. Kuzyk, T. Oo, G. L. Long, and H. Wang, "Chip-based silica microspheres for cavity
426   optomechanics," Optics Express **23**(21), 27260-27265 (2015).
427 17. T. Antoni, A. G. Kuhn, T. Briant, P.-F. Cohadon, A. Heidmann, R. Braive, A. Beveratos, I. Abram, L. L. Gratiet,
428   I. Sagnes, and I. Robert-Philip, "Deformable two-dimensional photonic crystal slab for cavity optomechanics,"
429   Opt. Lett. **36**, 3434-3436 (2011)
430 18. S. K. Manjeshwar, K. Elkhouly, J. M. Fitzgerald, et al., "Suspended photonic crystal membranes in AlGaAs
431   heterostructures for integrated multi-element optomechanics," Applied Physics Letters **116**(26), 264001 (2020).
432 19. J. Xia, Q. Qiao, G. Zhou, F. S. Chau, G. Zhou, "Opto-mechanical photonic crystal cavities for sensing application,"
433   Applied Sciences **10**(20), 7080 (2020).
434 20. P. K. Shandilya, J. E. Fröch, M. Mitchell, et al., "Hexagonal boron nitride cavity optomechanics," Nano Letters
435   **19**(2), 1343-1350 (2019).

21. J. Xia, F. Wang, C. Cao, Z. Hu, H. Yang, S. Xiong, "A nanoscale photonic crystal cavity optomechanical system for ultrasensitive motion sensing," Crystals **11**(5), 462 (2021).

22. H. Pfeifer, T. Paraïso, L. Zang, and O. Painter, "Design of tunable GHz-frequency optomechanical crystal resonators," Optics Express **24**(11), 11407-11419(2016).

23. L. Mercadé, L. L. Martín, A. Griol, D. Navarro-Urrios, and A. Martínez, "Microwave oscillator and frequency comb in a silicon optomechanical cavity with a full phononic bandgap," Nanophotonics **9**(11), 3535-3544 (2020).

24. L. Schwab, P. E. Allain, N. Mauran, X. Dollat, L. Mazenq, D. Lagrange, and B. Legrand, "Very-high-frequency probes for atomic force microscopy with silicon optomechanics," Microsystems & Nanoengineering **8**(1), 1-14 (2022).

25. A. de los Ríos Sommer, N. Meyer, and R. Quidant, "Strong optomechanical coupling at room temperature by coherent scattering," Nature Communications **12**(1), 1-7 (2021).

26. S. M. Meenehan, J. D. Cohen, S. Gröblacher, J. T. Hill, A. H. Safavi-Naeini, M. Aspelmeyer, and O. Painter, "Silicon optomechanical crystal resonator at millikelvin temperatures," Physical Review A **90**(1), 011803 (2014).

27. E. Serra, B. Morana, A. Borrielli, F. Marin, G. Pandraud, A. Pontin, and M. Bonaldi, "Silicon nitride MOMS oscillator for room temperature quantum optomechanics," Journal of Microelectromechanical Systems **27**(6), 1193-1203 (2018).

28. X. Lu, J. Y. Lee, and Q. Lin, "Silicon carbide zipper photonic crystal optomechanical cavities," Applied physics letters **116**(22), 221104 (2020).

29. V. Villafañe, S. Anguiano, A. E. Bruchhausen, G. Rozas, J. Bloch, C. G. Carbonell, A. Lemaître, and A. Fainstein, "Quantum well photoelastic comb for ultra-high frequency cavity optomechanics," Quantum Science and Technology **4**(1), 014011 (2018).

30. S. Kobtsev, D. Radnatarov, S. Khripunov, I. Popkov, V. Andryushkov, and T. Steshchenko, "Stability properties of an Rb CPT atomic clock with buffer-gas-free cells under dynamic excitation," JOSA B **36**(10), 2700-2704 (2019).

31. T. B. Beyazoglu, "Integrated MEMS cavity optomechanical oscillators for wireless and optical communications," PhD thesis, UC Berkeley (2016).

32. F. Lienhart, S. Boussen, O. Carraz, N. Zahzam, Y. Bidel, and A. Bresson, "Compact and robust laser system for rubidium laser cooling based on the frequency doubling of a fiber bench at 1560 nm," Appl. Phys. B: Lasers Opt. 89, 177–180 (2007).

33. Y. Sortais, S. Bize, C. Nicolas, A. Clairon, C. Salomon, and C. Williams, "Cold collision frequency shifts in a 87Rb atomic fountain," Phys. Rev. Lett. 85(15), 3117–3120 (2000).

34. E. Saglamyurek, J. Jin, V. B. Verma, M. D. Shaw, F. Marsili, S. W. Nam, D. Oblak and W. Tittel, "Quantum storage of entangled telecom-wavelength photons in an erbium-doped optical fibre," Nature Photonics, 9, 83–87 (2015).

35. C. T. C. Nguyen, J. Kitching, "Towards chip-scale atomic clocks," IEEE International Solid-State Circuits Conference (ISSCC), 84-85 (2005).

36. C. T. C. Nguyen, "MEMS technology for timing and frequency control," IEEE Transactions on Ultrasonics, Ferroelectrics, and Frequency Control, 54(2), 251-270(2007).

37. Tanimura, Takahito, et al. "Generation of a squeezed vacuum resonant on a rubidium D1 line with periodically poled KTiOPO4," Optics Letters, 31, 2344-2346 (2006).

38. Z. Chen, Q. Xu, K. Zhang, W.-H. Wong, D.-L. Zhang, E. Y.-B. Pun, and C. Wang, "Efficient erbium-doped thin-film lithium niobate waveguide amplifiers," Opt. Lett. **46**, 1161-1164 (2021).

39. R. Gao, B. Fu, N. Yao, et al., "Electro-optically tunable low phase-noise microwave synthesizer in an active lithium niobate microdisk," arXiv preprint arXiv:2209.10782 (2022).

40. M. Li, J. Ling, Y. He, et al., "Lithium niobate photonic-crystal electro-optic modulator," Nature Communications **11**, 4123 (2020).

41. J. Zhang, B. Pan, W. Liu, D. Dai, and Y. Shi, "Ultra-compact electro-optic modulator based on etchless lithium niobate photonic crystal nanobeam cavity," Optics Express, **30**(12), 20839-20846 (2022).

42. Y. Liu, X. Yan, J. Wu, et al., "On-chip erbium-doped lithium niobate microcavity laser," Sci. China Phys. Mech. Astron. **64**, 234262 (2021).

43. H. Liang, R. Luo, Y. He, H. Jiang, and Q. Lin, "High-quality lithium niobate photonic crystal nanocavities," Optica **4**, 1251-1258 (2017).

44. M. Li, H. Liang, R. Luo, Y. He, and Q. Lin, "High-Q 2D lithium niobate photonic crystal slab nanoresonators," Laser & Photonics Reviews **13**(5), 1800228 (2019).

45. W. C. Jiang, and Q. Lin, "Chip-scale cavity optomechanics in lithium niobate," Scientific Reports **6**(1), 1-7 (2016).

46. M. Shen, J. Xie, C.-L. Zou, Y. Xu, W. Fu, and H. X. Tang, "High frequency lithium niobate film-thickness-mode optomechanical resonator," Applied Physics Letters **117**(13), 131104 (2020).

47. A. Boes, B. Corcoran, L. Chang, J. Bowers, and A. Mitchell, "Status and potential of lithium niobate on insulator (LNOI) for photonic integrated circuits," Laser & Photonics Reviews **12**(4), 1700256 (2018).

48. T. Yamamoto, M. Notomi, H. Taniyama, E. Kuramochi, Y. Yoshikawa, Y. Torii, and T. Kuga, "Design of a high-Q air-slot cavity based on a width-modulated line-defect in a photonic crystal slab," Optics Express **16**(18), 13809-13817 (2008).

49. Y. Li, J. Zheng, J. Gao, J. Shu, M. S. Aras, and C. W. Wong, "Design of dispersive optomechanical coupling and cooling in ultrahigh-Q/V slot-type photonic crystal cavities," Optics Express **18**(23), 23844-23856 (2010).

50. Y. Huang, J. G. F. Flores, Z. Cai, J. Wu, M. Yu, D. L. Kwong, and C. W. Wong, "Controllable optomechanical coupling and Drude self-pulsation plasma locking in chip-scale optomechanical cavities," Optics Express **25**(6), 6851-6859 (2017).

51. A. F. Oskooi, D. Roundy, M. Ibanescu, et al. "MEEP: A flexible free-software package for electromagnetic simulations by the FDTD method," Computer Physics Communications **181**(3): 687-702 (2010).

52. K. S. Yee, "Numerical solution of initial boundary value problems involving Maxwells equations in isotropic media," IEEE Transactions on Antennas and Propagation **14**(3), 302-307 (1966).

53. D. S. Smith, H. D. Riccius, R. P. Edwin, "Refractive indices of lithium niobate," Optics Communications **17**(3), 332-335 (1976).

54. Y. Li, K. Cui, X. Fang, Y. Huang, Z. Huang, F. Liu, and W. Zhang, "Optomechanical crystal nanobeam cavity with high optomechanical coupling rate," Journal of Optics **17**(4), 045001 (2015).

55. J. Chan, "Laser cooling of an optomechanical crystal resonator to its quantum ground state of motion," PhD thesis, California Institute of Technology (2012).